Acta Cryst. (1996). A52, 427–437

The Non-Resonant Magnetic X-ray Scattering Cross Section of MnF_2. 1. Medium X-ray Energies from 5 to 12 keV

T. BRÜCKEL,[a,b]* M. LIPPERT,[b] T. KÖHLER,[b] J. R. SCHNEIDER,[b] W. PRANDL,[a] V. RILLING[a] AND M. SCHILLING[a]

[a]*Institut für Kristallographie der Universität Tübingen, Charlottenstrasse 33, D-72070 Tübingen, Germany, and* [b]*Hamburger Synchrotronstrahlungslabor HASYLAB at Deutsches Elektronen-Synchrotron DESY, Notkestrasse 85, D-22607 Hamburg, Germany. E-mail: brueckel@desy.de*

(*Received 19 September 1995; accepted 15 January 1996*)

Abstract

To demonstrate the possibilities of non-resonant magnetic X-ray diffraction, data taken on the antiferromagnetic model system MnF_2 in a medium X-ray energy range from 5 to 12 keV are presented. An experimental set-up for the measurement of magnetic X-ray diffraction is introduced that employs a new design for a highly flexible polarization analyzer for synchrotron X-ray diffraction based on 90° Bragg reflection from a single crystal. The analyzer has been successfully tested on beamline W1 at HASYLAB by measuring the polarization of the primary photon beam and of the 400 charge peak of an MnF_2 single crystal. Subsequently, the analyzer was used to explore the polarization dependence of the non-resonant magnetic X-ray scattering cross section of this sample, complemented by measurements of the directional dependencies without polarization analysis. In the latter configuration, count rates as high as 3800 photons s^{-1} and a peak-to-background ratio of 160:1 were obtained. A method to determine the direction of the magnetic moments with respect to the crystalline axes is presented. The results give experimental support for the theoretical form of the non-resonant magnetic X-ray scattering cross section and at the same time provide a feasibility test for a general magnetic structure determination.

1. Introduction

Magnetic neutron diffraction has dominated the microscopical investigation of magnetic materials since the first magnetic structure determination by Shull, Strauser & Wollan (1951). The reasons for the superiority of thermal neutrons as a probe for magnetic structures and excitations lie not only in the microscopical space and time resolution but also in the direct coupling of the neutron dipolar moment with the atomic magnetic moments of the sample (*e.g.* Rossad-Mignod, 1987). The strength of this interaction is comparable to the interaction of the neutron with the nuclei, resulting in similar intensities for magnetic and nuclear scattering. This is in complete contrast to the scattering of X-rays from condensed matter. As with thermal neutron scattering, a microscopical space resolution can be obtained since in both cases the wavelength is comparable to the interatomic distances. Owing to the high incident energy (several keV as compared to characteristic excitation energies of some meV), measurements with microscopic energy resolution are difficult (Burkel, 1991) and will certainly remain impossible for magnetic excitations for many years to come. In addition, magnetic scattering, as a relativistic effect, is largely suppressed as compared to regular charge (Thomson) scattering. For the scattering amplitude $S(\mathbf{Q})$, the ratio between magnetic and charge scattering amounts roughly to (see *e.g.* Blume, 1985; Brunel & de Bergevin, 1991; Gibbs, 1992)

$$S_{\rm mag}(\mathbf{Q})/S_{\rm charge}(\mathbf{Q}) \simeq (\hbar\omega/mc^2)2\sin\theta(N_M f_M/Nf)\langle S\rangle = (\lambda_C/d)(N_M f_M/Nf)\langle S\rangle. \quad (1)$$

Here, $\hbar\omega$ denotes the photon energy, mc^2 the rest mass of an electron (511 keV), θ the diffraction angle, N (N_M) and f (f_M) the number and the form factor of all (the magnetic) electrons, $\langle S\rangle$ the expectation value of the spin quantum number, d the lattice spacing and $\lambda_C = h/mc = 2.426$ pm, the Compton length of an electron. Using appropriate values for the parameters in (1), one finds that the intensity of magnetic scattering is typically six orders of magnitude smaller than the intensity of charge scattering. For this reason, magnetic X-ray scattering has been considered an exotic topic after its discovery in 1972 and further pioneering experiments by de Bergevin & Brunel (1972, 1981). Magnetic X-ray diffraction has become a real alternative to neutron diffraction only since the availability of highly intense, collimated, polarized and tunable X-ray beams provided by synchrotron-radiation sources. The main breakthrough came at the end of the 80s with magnetic X-ray diffraction studies of the rare-earth element Ho (Gibbs, Moncton, D'Amico, Bohr & Grier, 1985; Bohr, Gibbs, Moncton & D'Amico, 1986). Owing to the superior Q-space resolution, details of the magnetic structure, namely discommensurations or spin slips, could be resolved,

which had not been seen in earlier neutron diffraction experiments. Moreover, a first attempt was made to separate spin and orbital contributions to the magnetic form factor (Gibbs *et al.*, 1988), an experiment that is not feasible with neutrons because of the specific form of the cross section. For the first time, a resonance enhancement of the magnetic signal has been observed on Ho (Gibbs *et al.*, 1988) and could be theoretically described as resonant exchange scattering (Hannon, Trammell, Blume & Gibbs, 1988). Intensity gain factors of typically 50 are obtained for the lanthanide L_{II} and L_{III} edges. At the M_{IV} edge of actinides, this intensity gain can be as high as seven orders of magnitude (Isaacs *et al.*, 1989). Resonant diffraction also allows spectroscopy of the electronic states above the Fermi edge and renders magnetic diffraction sensitive to the magnetic species. With all the advantages of resonant diffraction, it is natural that thereafter only a few experiments dealt with non-resonant magnetic X-ray diffraction, mainly on the well characterized model antiferromagnet MnF_2 (Goldman *et al.*, 1987; Brückel *et al.*, 1993; Lippert, Brückel, Köhler & Schneider, 1994) or its site-diluted random field system $Mn_xZn_{1-x}F_2$ (Thurston, Peters, Birgeneau & Horn, 1988; Hill, Thurston, Erwin, Ramstad & Birgeneau, 1991; Hill, Feng, Birgeneau & Thurston, 1993*a*,*b*).

For transition-metal ions, only K edges lie in the range of hard X-ray wavelengths where atomic resolution is achievable. Owing to the dipole and quadrupole selection rules and the small overlap between core 1*s* states and the magnetic sensitive 3*d* or 4*p* energy bands, resonance enhancements are negligible at transition-metal K edges (Namikawa, Ando, Nakajima & Kawata, 1985). For example, at the K edge of MnF_2, the magnetic resonant scattering is completely dominated by resonant anomalous charge scattering (de Bergevin, Stunault, Vettier, Brückel & Lippert, 1993) while we found an enhancement by a factor of 2 in $RbMnF_3$ (Stunault, de Bergevin, Wermeille, Brückel & Vettier, 1994). For investigations of such materials, one is left with neutron or non-resonant magnetic X-ray scattering. Since most magnetic materials contain 3*d* elements, it is obvious that techniques for non-resonant magnetic X-ray scattering have to be developed for magnetic X-ray scattering to become a generally applicable microscopic probe of magnetism. Moreover, the non-resonant magnetic scattering cross section contains complementary information as compared to the resonant scattering cross section. For example, with non-resonant diffraction, the separation of spin and angular momentums should be possible without further assumptions and magnetic moment directions can be determined by the procedure outlined below. For these reasons, we decided to investigate the possibilities of non-resonant magnetic X-ray diffraction on the simple and very well characterized model system MnF_2. In contrast to an earlier X-ray study of MnF_2 (Goldman *et al.*, 1987), which concentrated on the temperature dependence of the order parameter close to the transition temperature T_N, we were mainly interested in the dependencies of the cross section on moment direction, magnitude of the scattering vector and polarization. The latter contains important information: polarization analysis can be used to distinguish between magnetic and charge scattering. In addition, it is essential for a systematic investigation of the various parts of the magnetic cross section. Off resonance, the Fourier components of spin and orbital angular momentum densities depend in different ways on the scattering geometry and the incident and final polarization states. Therefore, X-ray scattering can separate directly the different contributions to magnetization densities in solids. Examples for the application of polarization analysis to the non-resonant and resonant magnetic scattering from holmium can be found in Gibbs *et al.* (1988) and for the non-resonant scattering from $Mn_{0.75}Zn_{0.25}F_2$ in Hill, Feng, Birgeneau & Thurston (1993*b*). Polarization analysis is also important in anomalous anisotropic scattering experiments for the determination of extinction factors and in measurements of the Faraday effect (Belyakov & Dimitrienko, 1989).

The paper is organized as follows: Our magnetic model system MnF_2 is introduced in §2. Elements of the non-resonant magnetic scattering cross section relevant to this work are discussed in §3. In §4, we describe an experimental set-up that allows a full linear polarization analysis in a synchrotron X-ray diffraction experiment. Its main feature is a new polarization analyzer, which was constructed for applications in magnetic X-ray scattering. In §5, we report some test experiments that demonstrate the capabilities of the device and allow us to determine the polarization state of the incident X-ray beam. The results of our magnetic diffraction experiments on MnF_2 are presented in §6, followed by a discussion (§7) and summary and conclusions (§8). Parts of this work have already been published as a conference report (Brückel, Lippert, Köhler, Schneider & Prandl, 1995). First observations of magnetic scattering from MnF_2 at very high photon energies have been reported by Brückel *et al.* (1993) and Lippert, Brückel, Köhler & Schneider (1994). New and more detailed studies at 80 keV are the subject of the following paper (Strempfer *et al.*, 1996, hereafter referred to as paper 2).

2. The model system MnF_2

As explained in the *Introduction*, non-resonant magnetic X-ray diffraction is of particular interest in transition-metal compounds, where no resonance enhancement of the magnetic scattering can be obtained for hard X-rays. We have chosen MnF_2 as a model system because it has

been very well characterized by various techniques including neutron (Erickson, 1953) and X-ray scattering (Goldman *et al.*, 1987; Lippert, Brückel, Köhler & Schneider, 1994) and because crystals of excellent quality are available. The crystal used in our studies has the shape of a platelet with a (100) surface and dimensions $2 \times 10 \times 15$ mm. The mosaic distribution is anisotropic. For reflections of type $h00$, the rocking-curve width was determined by high-resolution scattering of 80 keV X-rays. With the c axis perpendicular to the scattering plane, we determined a width of 12″ for the mosaic distribution; with **c** in the scattering plane, the corresponding value is 20″.

Some basic properties of MnF_2 relevant for our work are listed below:

(*a*) MnF_2 has the simple tetragonal rutile-type crystal structure with space group $P4/mnm$ depicted in Fig. 1. Mn is located at the corners and the center of the tetragonal unit cell of dimensions $a = 4.874$ and $c = 3.310$ Å at room temperature. The Mn atom at $(0, 0, 0)$ is surrounded by a pair of nearest-neighbor F atoms at positions $\pm(0.305, 0.305, 0)$ (Jauch, Schneider & Dachs, 1983), while the local environment is rotated for the central Mn atom owing to the presence of the n-glide plane.

(*b*) Below $T_N \simeq 67.7$ K, MnF_2 orders antiferromagnetically as indicated in Fig. 1 (Erickson, 1953): MnF_2 is an example of a simple two-sublattice antiferromagnet, where the magnetic moment in the center of the unit cell is antiparallel to the moment at the corners. A small uniaxial anisotropy aligns the moments parallel to the $\pm c$ axis. Only two domain types exist and the domain sizes are macroscopical (Baruchel *et al.*, 1988), leading to resolution-limited widths of magnetic Bragg reflections for lattice-parameter scans. Since the spin direction relative to the lattice is well known, the dependence of the cross section on the various components of the magnetic moment can be investigated by turning the sample around the scattering vector as will be explained below in further detail.

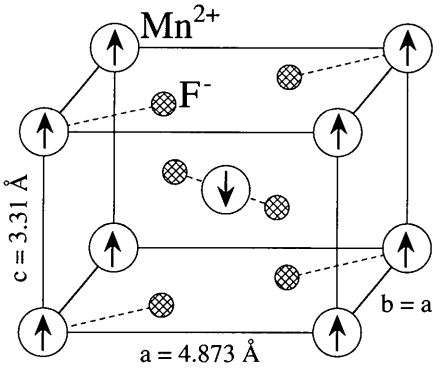

Fig. 1. The crystalline and magnetic unit cell of MnF_2

(*c*) Covalence effects are small (Nathans, Alperin, Pickart & Brown, 1963) so that the magnetic moment results mainly from a spherically symmetric ${}^6S_{5/2}$ state of the Mn^{2+} ion, *i.e.* is due to spin only. Therefore, only the spin-dependent part of the scattering cross section could be tested in our experiments.

(*d*) Because the chemical and magnetic unit cells coincide, there are reflections such as 111, 210,... that have both magnetic and charge contributions at low temperatures. However, owing to the glide plane (n in the paramagnetic phase for $T > T_N$, n' in the magnetically ordered phase for $T < T_N$, where the prime denotes the time-inversion operation) or the screw axis (4_2 for $T > T_N$, $4_2'$ for $T < T_N$), reflections of type $h00$ with $h = 2n + 1$ ($n = 0, 1, 2, 3, \ldots$) have no charge contribution either in the paramagnetic or in the ordered phase. Therefore, at these reciprocal-lattice points, the purely magnetic part of the cross section can be measured in principle. However, since charge scattering at $h00$ reflections is not forbidden by an integral reflection condition – as for centered unit cells – multiple charge scattering due to *Umweganregung* can occur and may obstruct the observation of the magnetic signal. Since magnetic scattering is much weaker than charge scattering, even weak multiple-scattering events due to weak charge reflections and streaks of the resolution function have to be avoided by rotating the sample around the scattering vector (Ψ angle). Multiple-scattering events can be identified by a calculation of their positions and usually experimentally by their intensity, shape and displacement in ω. This will be discussed in more detail in paper 2 for the scattering of high-energy photons, where the effect is much more important.

(*e*) At the Mn K edge, anisotropic anomalous (Templeton) scattering may occur and can give rise to the appearance of intensity for reflections being systematically extinct by space-group symmetry. This effect occurs for reflections of type $h00$, where the extinction condition due to the n- (n'-) glide plane is violated at resonance (Kirfel, Petcov & Eichhorn, 1991), leading to intensities roughly three orders of magnitude larger than purely magnetic scattering. Therefore, a wide energy region of some 400 eV around the Mn K edge should be avoided in studies of non-resonant magnetic diffraction.

3. The non-resonant magnetic X-ray scattering cross section

The cross section for non-resonant magnetic X-ray scattering has been discussed in various approximations by several authors (de Bergevin & Brunel, 1981; Platzman & Tzoar, 1970; Grotch, Kazes, Bhatt & Owen, 1983; Blume, 1985; Blume & Gibbs, 1988; Lovesey, 1987). For the case of diffraction of high-energy X-rays, the limitations of these approximations

become apparent and will be discussed in paper 2. Here we recall the basic results in a formulation adapted to the specific case of Bragg diffraction. At moderately high X-ray energies, the elastic cross section for scattering of photons with incident polarization ε into a state of final polarization ε' can be written as

$$\mathrm{d}\sigma/\mathrm{d}\Omega\big|_{\varepsilon\to\varepsilon'} = [e^2/mc^2]^2 \left|\langle M_C\rangle_{\varepsilon'\varepsilon} + i(\lambda_C/d)\langle M_M\rangle_{\varepsilon'\varepsilon}\right|^2. \tag{2}$$

Here, $r_e = e^2/mc^2 \simeq 2.818\,\mathrm{fm}$ denotes the classical electron radius, $\lambda_C = h/mc = 2.426\,\mathrm{pm}$, the Compton length of an electron. The scattering amplitudes $\langle M_C\rangle$ and $\langle M_M\rangle$ are given as matrices that describe the polarization dependencies of charge and magnetic scattering, respectively. In our experiment, we used linearly polarized photons from a symmetric wiggler and measured the components of the linear polarization after scattering. It is therefore convenient to use as basis vectors, for a description of the photon polarization, unit vectors perpendicular to the wave vectors of incident and scattered photons, $\mathbf{k}$ and $\mathbf{k}'$. σ polarization corresponds to the basis vector perpendicular to the scattering plane, π polarization corresponds to the vectors in the $\mathbf{kk}'$ plane. The basis vectors for the components of the magnetic moment of the sample and for the polarization states are plotted in Fig. 2 and defined as follows:

$$\begin{aligned}
\hat{\mathbf{u}}_1 &= (\mathbf{k}+\mathbf{k}')/|\mathbf{k}+\mathbf{k}'|,\\
\hat{\mathbf{u}}_2 &= (\mathbf{k}'\times\mathbf{k})/|\mathbf{k}'\times\mathbf{k}| \equiv \sigma \equiv \sigma',\\
\hat{\mathbf{u}}_3 &= (\mathbf{k}'-\mathbf{k})/|\mathbf{k}'-\mathbf{k}| = \mathbf{Q}/Q,\\
\boldsymbol{\pi} &= \hat{\mathbf{k}}\times\boldsymbol{\sigma}, \quad \boldsymbol{\pi}' = \hat{\mathbf{k}}'\times\boldsymbol{\sigma}'.
\end{aligned} \tag{3}$$

Note that compared to Blume & Gibbs (1988) we chose the opposite sign for the basis vectors $\hat{\mathbf{u}}_2$ and $\hat{\mathbf{u}}_3$ since we like to keep the usual definition of the scattering vector $\mathbf{Q} = \mathbf{k}' - \mathbf{k} \parallel \hat{\mathbf{u}}_3$. In this basis, the matrices in (2) can be written as:

(*a*) $\langle M_M\rangle$ for the magnetic part:

from / to	σ	π
σ'	$S_2\cos\theta$	$[(L_1+S_1)\cos\theta + S_3\sin\theta]\sin\theta$
π'	$[-(L_1+S_1)\cos\theta + S_3\sin\theta]\sin\theta$	$[2L_2\sin^2\theta + S_2]\cos\theta;$

(4)

(*b*) $\langle M_C\rangle$ for charge scattering:

from / to	σ	π
σ'	$\rho(\mathbf{Q})$	0
π'	0	$\rho(\mathbf{Q})(\cos 2\theta).$

(5)

Here, $S_i = S_i(\mathbf{Q})$ and $L_i = L_i(\mathbf{Q})$ $(i = 1, 2, 3)$ denote the components of the Fourier transform of the magnetization density due to the spin and orbital angular momentum, respectively, as defined in Blume & Gibbs (1988). $\rho(\mathbf{Q})$ denotes the Fourier transform of the electronic charge-density distribution.

We would like to add some comments to the form of the cross section given in (2) to (5):

(*a*) Magnetic scattering is a relativistic correction to charge scattering and therefore the cross section (2) is usually written in a slightly different form with a pre-factor $\hbar\omega/mc^2$ for the magnetic amplitude. This form shows that for observations under a given scattering angle the amplitude of magnetic scattering increases with photon energy since relativistic effects became pronounced as $\hbar\omega \to mc^2$. Using this pre-factor is therefore well adapted to the case of incoherent Compton scattering. For coherent elastic Bragg scattering, on the other hand, the ratio between the magnetic and the charge amplitudes is determined by the momentum transfer and not by the energy transfer. Therefore, we have written the pre-factor for the magnetic amplitude in the cross section (2) as λ_C/d [and included a factor $(2\sin\Theta)^{-1}$ in $\langle M_M\rangle$], which emphasizes that for a given Bragg reflection the ratio between magnetic and charge scattering is virtually independent of photon energy, at least to within the approximations leading to (2).

(*b*) Equation (2) contains three terms: pure Thomson scattering $(\sim |\langle M_C\rangle|^2)$, purely magnetic scattering $[\sim |(\lambda_C/d)\langle M_M\rangle|^2]$ and an interference term $[\sim -2(\lambda_C/d)\mathrm{Im}\{\langle M_C\rangle\langle M_M\rangle^*\}]$. The latter vanishes if charge and magnetic scattering do not occur at the same position in reciprocal space. Only this case is relevant in what follows, *i.e.* we consider pure magnetic scattering only.

(*c*) Equation (4) shows that the spin and orbital contributions have different angular and polarization dependencies and can therefore be distinguished in principle. However, for the case of MnF_2, we have to deal with the spin part only.

(*d*) The components S_2 and L_2 perpendicular to the scattering plane do not alter the photon polarization during scattering for a pure incident state, while the components in the scattering plane always induce

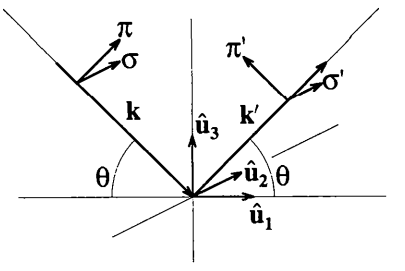

Fig. 2. Definition of the basis vectors for the components of the spin and angular momentum as well as for the polarization states of the incident and diffracted beams.

transitions $\sigma \longleftrightarrow \pi$. The latter processes can be used to distinguish between magnetic and charge scattering.

The form of the scattering cross section (2) is only valid for a totally ε polarized beam. For the general case of a mixed polarization state, a density-matrix formalism is appropriate. This is discussed in detail by de Bergevin & Brunel (1981) and Blume & Gibbs (1988). Here we restrict ourselves to the case for our experimental situation, where we have an incident beam with linear polarization

$$P = (|E_\sigma|^2 - |E_\pi|^2)/(|E_\sigma|^2 + |E_\pi|^2) > 0 \qquad (6)$$

along the $\hat{\mathbf{u}}_2$ axis and all other components vanish [E_π and E_σ represent the components of the electric field vector along the two orthogonal basis vectors defined in (3)]. In this case, the density matrix for the incident beam takes the very simple form

$$\boldsymbol{\rho} = \frac{1}{2}\begin{pmatrix} 1+P & 0 \\ 0 & 1-P \end{pmatrix}. \qquad (7)$$

With (7), the density matrix of the final beam and the scattering cross section can then be calculated as

$$\boldsymbol{\rho}' = \langle M\rangle\boldsymbol{\rho}\langle M\rangle^\dagger; \quad \mathrm{d}\sigma/\mathrm{d}\Omega = (e^2/mc^2)^2\,\mathrm{tr}(\boldsymbol{\rho}'). \qquad (8)$$

We further consider only the spin part of the purely magnetic scattering cross section and assume $S_3 = 0$, which is appropriate for our actual experimental configuration, see below. Then we obtain from (8):

$$\mathrm{d}\sigma/\mathrm{d}\Omega = (e^2/mc^2)^2(\lambda_C/d)^2 \times \cos^2\theta\{[S_2(\mathbf{Q})]^2 + [S_1(\mathbf{Q})]^2\sin^2\theta\}, \qquad (9)$$

$$P' = P(S_2^2 - S_1^2\sin^2\theta)/(S_2^2 + S_1^2\sin^2\theta), \qquad (10)$$

where $P' = (|E_{\sigma'}|^2 - |E_{\pi'}|^2)/(|E_{\sigma'}|^2 + |E_{\pi'}|^2)$ again denotes the degree of linear (σ', π') polarization after diffraction. In our experiment, we only measured this component.

4. Experimental set-up for magnetic X-ray diffraction and linear polarization analysis

The experiments were done on the wiggler beamline W1 at HASYLAB with the storage ring DORIS operating at 4.5 GeV positron energy. The X-ray source is a 32 pole wiggler with a critical energy of 8.1 keV at minimal gap. The main optical components of this beamline are a fixed-exit double monochromator and a double-focusing Au-coated toroidal mirror. For our experiments, we employed water-cooled Si(111) monochromator crystals. To monitor the incident intensity and polarization, we used an ionization chamber and a polarization monitor, respectively. The sample is mounted inside a closed-cycle cryostat that allows temperature variations between 10 and 300 K with a temperature stability better than 1 K. In a first experiment, the cryostat was equipped with an internal cold sample rotation and Kapton windows (Ihringer & Küster, 1993), while in a second experiment Be domes allowed a rotation of the cryostat as a whole. The cryostat is attached to a RISØ-type surface diffractometer and three goniometers provide for all angular degrees of freedom. Finally, the scattered beam can be measured either directly with an NaI scintillation detector or with a Ge solid-state detector. A new analyzer/polarization analyzer unit, which is described in more detail below, can also be employed.

The polarization monitor is based on the polarization dependence of charge scattering (5) and measures the linear polarization P defined in (6). Note that from a symmetric wiggler we do not expect any circular polarized component or linear polarization at 45° with respect to the σ and π directions. Two NaI scintillation counters are mounted with their axes perpendicular to each other and to the incident beam. Collimators in front of the detectors select scattering in a narrow angular range around the σ and π directions, respectively. In contrast to the set-up proposed by Smend, Schaupp, Czerwinski, Millhouse & Schenk-Strauss (1985), we did not use a Kapton foil as scatterer, since it turned out that such a device is rather sensitive to the alignment in the beam. Instead, we used air scattering, which gave sufficient count rates to obtain P with a precision of 1% within 1 s.

The polarization analyzer is again based on 90° charge scattering, but this time from a single crystal to enhance the diffracted intensity [compare the set-up described by Gibbs, Blume, Harshman & McWhan (1989)]. Our new design stands out for its high versatility. With the same device, the diffracted beam from the sample can be detected without further analysis and, after scattering from an analyzer crystal, in the conventional set-up to enhance the energy and Q-space resolution of the diffractometer or as a polarization analyzer to measure the degree of linear polarization after scattering from the sample. A sketch of the device is shown in Fig. 3. The diffracted beam from the sample passes through an evacuated flight tube, which serves as a collimator owing to the two cross-slit systems in front and behind the tube. In order to select a certain region on the sample surface, the first slits are stepper-motor driven and can be scanned in two perpendicular directions. The flight tube together with the following analyzer unit is mounted on a base plate that allows for three manual adjustments (one translation and two rotations). These are needed to align the incident wave vector of the analyzer unit ($\mathbf{k}_A$) with the final wave vector from the sample ($\mathbf{k}'$), which has to be done at the beginning of each experiment. The analyzer unit itself is mounted inside two perpendicular aluminium tubes in a T-shaped arrangement. The aluminium housing provides very good shielding so that the analyzer is virtually background free. The central tube is mounted

on a turntable that allows the analyzer unit to rotate around ($\mathbf{k}_A$) (angle α). This feature is required for use as a polarization analyzer with 90° scattering from the analyzer crystal. For example, by changing α, the beam can be scattered from the analyzer crystal either within the scattering plane of the sample or perpendicular to it, giving access to the σ and π components of the diffracted beam, respectively. The perpendicular tube of the 'T' has two gionometers on either side, one for the detector arm ($2\Theta_A$) and one for the analyzer crystal (ω_A), for which an additional tilt table is mounted on top of the ω_A movement. To further reduce the background, a double slit in front of the detector is available.

While for a conventional analysis perfect silicon or germanium crystals are used in order to achieve better energy and Q-space resolution, the requirements for an analyzer crystal are quite different for the case of polarization analysis, where integrated intensities are determined. Most important of all, one has to find a crystal with a reflection at $d = \lambda/2^{1/2}$, allowing for 90° diffraction. At $2\Theta_A = 90°$, the form factor and the Debye–Waller factor strongly reduce the reflected intensity. Therefore, the analyzer crystal should have a very high peak reflectivity. On the other hand, it should accept the whole divergence of the beam diffracted from the sample in order to avoid time-consuming rocking-curve scans of the analyzer crystal. Moreover, if the 90° condition cannot be kept ideally (note that the error in P' is less than 1% in the angular range 86 to 94°), the crystal should reflect kinematically

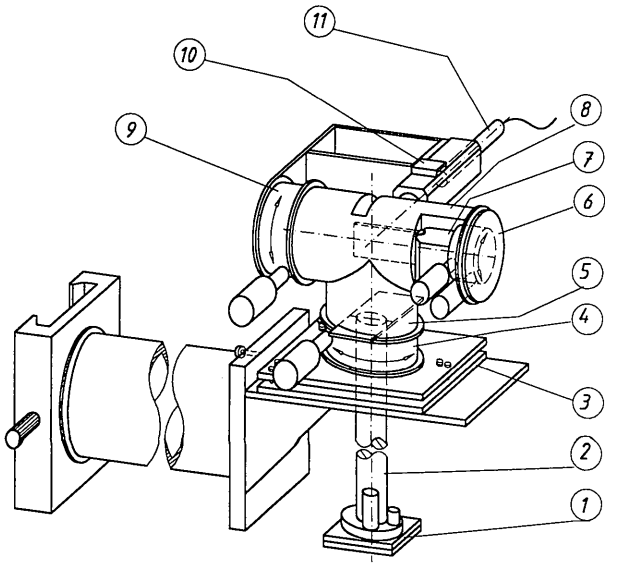

Fig. 3. Polarization analyzer. 1: motorized double slit system; 2: evacuated flight tube; 3: base plate with three manual degrees of freedom for alignment; 4: goniometer for the α movement (see text); 5: entrance slit; 6: goniometer for the ω movement of the analyzer crystal; 7: tilt of the analyzer crystal; 8: aluminium housing of the analyzer; 9: goniometer for the analyzer 2θ movement; 10: detector aperture slits; 11: NaI detector.

in order to allow for a correction of the measured polarization *via* (5). Therefore, the best choice is a mosaic crystal, which compromises between high peak reflectivity and a sufficient width of the rocking curve. Often, pyrolytic graphite (PG 002 and higher harmonics) is chosen as analyzer, which, however, gives only a very limited choice of wavelengths. In our experiments, we have successfully employed annealed silicon crystals with a mosaic width of $\sim 6''$ (Schneider *et al.*, 1989). Their high peak reflectivities partly compensate for the fact that the rocking-curve width is much too small to accept the full divergence of the beam in all directions ($\sim$ 50 to 10″). Much time can be saved by continuously sweeping the analyzer crystal through the diffraction condition instead of taking full rocking-curve step scans. While the mosaicity is still by far too small, the advantage of using annealed silicon crystals is that for many wavelengths between 1 and 2 Å there are main reflections that obey the 90° diffraction condition approximately.

5. Test of the polarization analyzer and the polarization of the incident synchrotron beam

For a first test of the polarization analysis set-up, we produced a completely σ-polarized beam by a close to 90° charge reflection from the sample crystal. As analyzer, we used a silicon 004 mosaic crystal for a wavelength of 1.91 Å. As expected, the degree of polarization of the diffracted beam turned out to be higher than 98%. In a second step, the polarization of the W1 primary beam was measured, once with the Si 004 analyzer for $\lambda = 1.91$ Å, once with PG 008 for $\lambda = 1.19$ Å. In Fig. 4, we plot integrated intensities from the PG 008 analyzer as a function of the angle α between the vertical and the scattering plane of the analyzer. The solid curve is a refinement according to

$$I(\alpha) = H\cos^2(\alpha - \alpha_0) + V\sin^2(\alpha - \alpha_0). \qquad (11)$$

H and V denote the intensities corresponding to horizontal and vertical polarization, respectively, and α_0 describes a possible tilt, which turned out to be identical to zero. The degree of horizontal polarization is given by [compare with (6)]

$$P = (H - V)/(H + V). \qquad (12)$$

With completely open entrance slits, we determined P to be about 84 (1)%. Here, we want to mention that all the measurements reported in this section have been done with the Si 111 double monochromator tuned to maximal intensity. Owing to dynamical diffraction effects, the polarization can be further increased by detuning the monochromator.

The value for P was verified by independent measurements with the polarization monitor. Fig. 5 shows the variation of the incident polarization with photon energy as determined from (12). The polariza-

tion of the full monochromatic beam is nearly independent of energy and amounts to roughly 85%. The polarization of the white beam in front of the monochromator is significantly lower. It has been calculated using the known machine parameters of the storage ring DORIS and insertion device (Pflüger, 1989). The result is shown in Fig. 5 as a dotted line. The double monochromator increases the polarization. For an ideal mosaic crystal with vertical scattering plane, the vertical component is suppressed by a factor $\cos^2\Theta$ [compare with (5)]. This factor holds only within the kinematical theory and not for dynamical diffraction (Jennings, 1981), which one would expect to occur for our perfect Si 111 monochromator crystals. However, the first monochromator crystal deforms under the thermal load of nearly 1 kW and thus no longer reflects as a truly perfect crystal. In total, we found that with an effective factor of $\cos^3 2\Theta$ for the suppression of the vertical (π) polarization component by our two monochromator crystals, we obtain a reasonable agreement between calculated and measured degree of polarization, see solid line in Fig. 5. Finally, we have examined the angular dependence of the linear polarization by performing a vertical scan with a fine slit of 0.2 mm. Fig. 6 shows the degree of linear polarization as a function of the angle of elevation above and below the orbital plane of the storage ring. The dots represent the measured values, the solid line the calculation, the difference probably being due to heat-load effects in the first crystal. As expected, the polarization can be increased up to 93% by closing the monochromator entrance slits vertically down to 1 mm. Without a polarizer (*e.g.* detuned monochromator crystals), a higher polarization cannot be obtained at the DORIS III storage ring owing to the finite vertical emittance of the electron beam, leading to a vertical beam dimension of $\sigma_z = 0.42$ mm with a divergence of $\sigma_z' = 0.033$ mrad at W1.

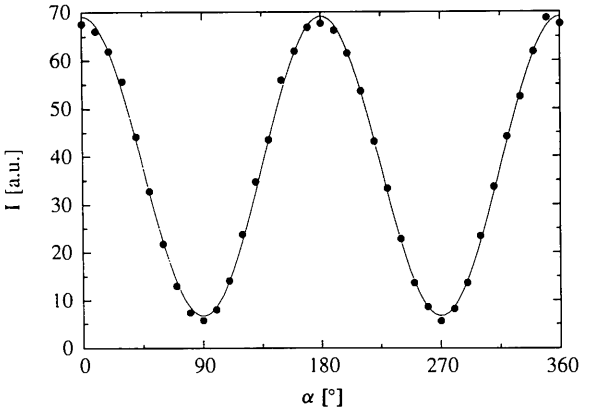

Fig. 4. Measurement of the polarization of the monochromatic primary beam with an energy of 10.46 keV. The full circles show integrated intensities I from a PG 008 analyzer as a function of the angle α described in the text. The solid line is a refinement according to equation (11).

6. Non-resonant magnetic scattering from MnF_2

We studied non-resonant magnetic diffraction from MnF_2 from the 100, 300 and 500 Bragg peaks at various X-ray energies between 5 and 12 keV below as well as above the Mn K edge. Fig. 7 shows a rocking curve of the 300 reflection from MnF_2 at $T = 10$ K and $\lambda = 1.5$ Å as an example. For this scan, the spin (*i.e.* the c axis) was perpendicular to the scattering plane ($S_1 = S_3 = 0$, $S_2 = S \simeq 5/2$) and we expect the diagonal elements in (4) to be maximized and the off-diagonal elements to vanish. Depending on the ring

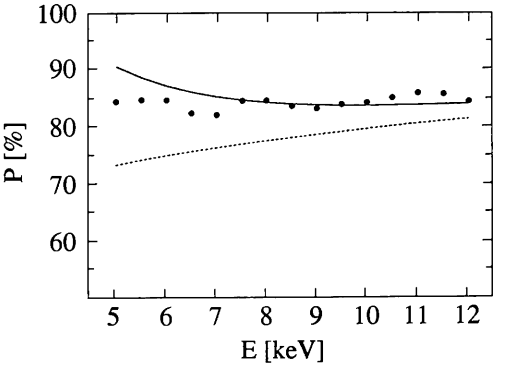

Fig. 5. Energy dependence of the linear polarization P of the full primary beam. The full circles show experimental data (with a typical standard deviation of ±1%) as measured with the polarization monitor according to the definition (12). The dotted line shows the expected linear polarization from the insertion device in front of the double monochromator. The monochromator increases the degree of linear polarization as indicated by the solid line. As a result, the degree of linear polarization at the sample becomes nearly independent of energy and amounts to ~85%.

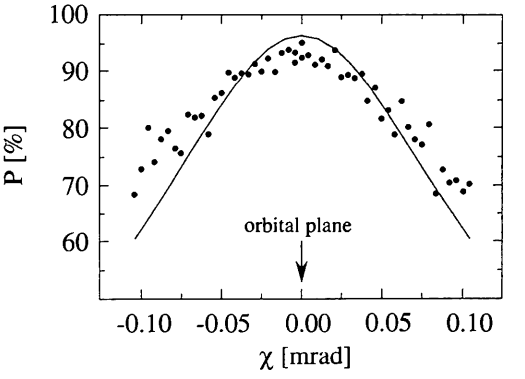

Fig. 6. Degree of linear polarization P as measured with the polarization monitor as a function of the angle of elevation χ above and below the orbital plane of the storage ring. The dots represent measured data, the solid line the calculated dependence.

current, a peak count rate of up to 3800 counts s^{-1} for non-resonant magnetic scattering could be observed. With a Ge detector, a peak-to-background ratio of 70:1 was obtained. Further improvements can be achieved by using an analyzer crystal as demonstrated in Fig. 8. We obtained a peak-to-background ratio of 160:1 with a Q-space resolution element of 5×10^{-9} Å^{-3}.

A first indication for the magnetic origin of the observed Bragg peaks is the temperature dependence shown in Fig. 9: above $T_N \simeq 68$ K, the Bragg signal vanishes completely. In a next step, we tested the dependencies of the magnetic cross section (4) on the spin components. Since the crystal has a (100) face and we are looking at $h00$ reflections, the crystal can be rotated around the scattering vector $\mathbf{Q}$ (angle ψ) without violating the Bragg condition or changing the scattering geometry. Since the spin is pointing towards $\pm\mathbf{c}$, the spin components during such a rotation are given by

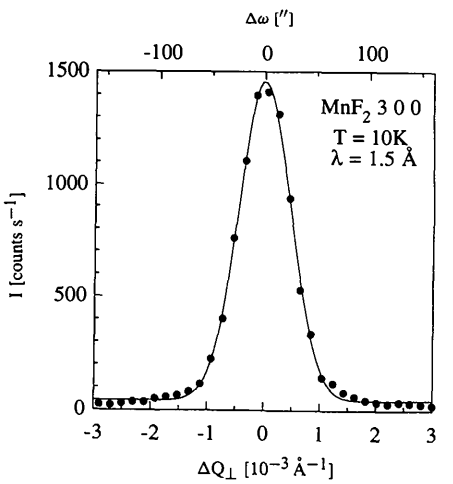

Fig. 7. Rocking curve of the 300 magnetic reflection at $T = 10$ K and $\lambda = 1.5$ Å. The spin is perpendicular to the scattering plane.

$$S_1 = S\sin\psi, \quad S_2 = S\cos\psi, \quad S_3 = 0, \tag{13}$$

and from (9) and (10) we obtain an expression for the variation of the integrated intensity (without polarization analysis) and for the degree of polarization in the form

$$I(\psi,\theta) \propto S^2(\cos^2\theta/d^2)(\cos^2\psi + \sin^2\psi\sin^2\theta) \tag{14}$$

$$P'(\psi,\theta) = P(\cos^2\psi - \sin^2\psi\sin^2\theta) \times (\cos^2\psi + \sin^2\psi\sin^2\theta)^{-1}. \tag{15}$$

Fig. 10 shows the measured integrated Bragg intensities for the 300 Bragg peak at $\lambda = 1.36$ Å as a function of ψ together with a refinement according to (14), where an overall scale factor was the only free parameter. The main difficulty in obtaining this curve is to avoid multiple Bragg diffraction, a problem that will be discussed in detail in paper 2 (Strempfer *et al.*, 1996). We mention that a similar experiment has been carried out by Brunel & de Bergevin (1981) on Fe_2O_3.

Fig. 11 shows a test of the polarization dependence. Following (15), we expect $P' = P$ for $\psi = 0$ and $P' = -P$ for $\psi = 90°$, *i.e.* for incident σ polarization as was the case in our experiment, $\sigma \rightarrow \sigma$ scattering should occur for $\psi = 0$ and $\sigma \rightarrow \pi$ for $\psi = 90°$. Our observations in Fig. 11 agree well with these predictions. Similar measurements have been reported for an $Mn_{0.75}Zn_{0.25}F_2$ sample by Hill *et al.* (1993*b*).

7. Discussion

Our results for the peak intensity and the peak-to-background ratio compare quite favorably to earlier measurements on MnF_2 (Goldman *et al.*, 1987) and show that non-resonant magnetic X-ray diffraction can be a very useful tool for studies of magnetic phase transitions, disorder phenomena and subtle structural

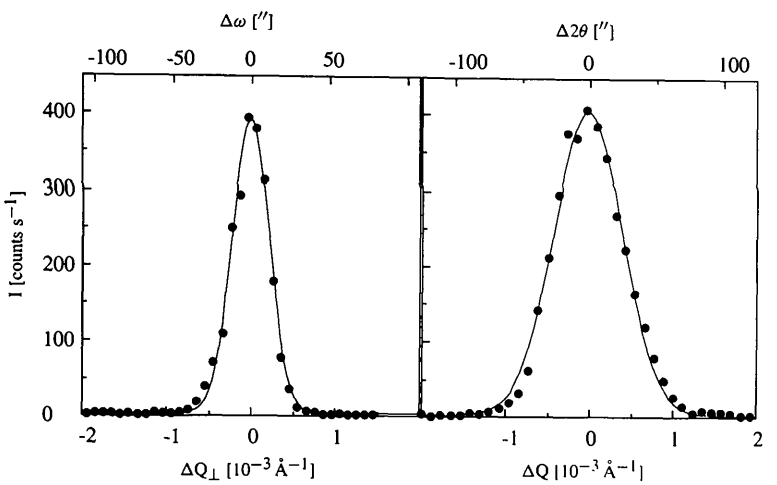

Fig. 8. Sample (left) and analyzer (right) scan of the 300 magnetic Bragg peak at $T = 10$ K and $\lambda = 1.9$ Å. The spin is perpendicular to the scattering plane. The analyzer crystal is Si 111.

details. First applications of non-resonant magnetic X-ray diffraction have indeed already been reported. A major advantage of magnetic X-ray diffraction with respect to magnetic neutron diffraction lies in the superior Q-space resolution demonstrated in Fig. 8. The value of 5×10^{-9} Å^{-3} for the resolution volume element has to be compared with typical values of 10^{-4} Å^{-3} in neutron diffraction. It should, however, be emphasized that the good intrinsic resolution is only advantageous for very good single crystals: non-resonant magnetic X-ray diffraction depends crucially on the crystal quality!

The main result of our investigation is shown in Fig. 10, which provides a test of the angular dependencies of the non-resonant magnetic X-ray scattering cross section (4). The ratio between $I(\psi = 0)$ and $I(\psi = 90°)$ is given by $\sin^2\theta = 0.17$ as predicted by (4). Moreover, the dependence on the spin components S_1 and S_2 could be confirmed. While the angular dependencies can be measured without polarization analysis, it is important to confirm that the polarization state of the scattered photons corresponds to the predictions of (4). This has been done by measurements utilizing our polarization analyzer as shown in Fig. 11. For magnetic diffraction, $\sigma \rightarrow \sigma$ scattering occurs if the spin is perpendicular to the scattering plane, while only $\sigma \rightarrow \pi$ scattering is present if the spin moment lies within the scattering plane. Only in the latter case do we observe a 'flip' of the polarization state, which allows magnetic scattering to be distinguished from charge scattering. The polarization analysis shown in Fig. 11 together with the angular dependencies from Fig. 10 provide a test of the spin-dependent part of the first column in (4). In our case, everything is known about the model system MnF_2. For a substance with unknown magnetic structure, on the other hand, an examination of the angular dependencies similar to that shown in Fig. 10 can reveal the spin direction relative to the lattice. Of course, this method only works for crystals where one spin direction is favored. This is the case for collinear magnetic structures and single-domain crystals or at least crystals with an uneven domain population.

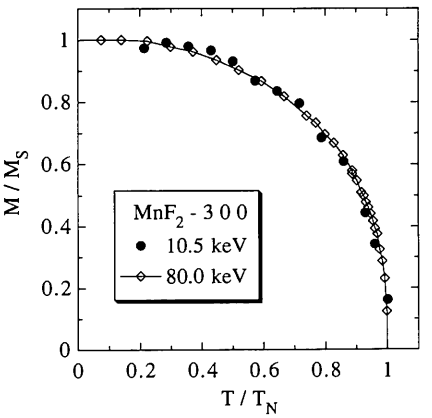

Fig. 9. Temperature dependence of the sublattice magnetization in reduced coordinates as obtained from the integrated intensity of the magnetic 300 reflection. The measurement at a photon energy of 10.5 keV (full circles) agrees well with a measurement at 80 keV (diamonds) reported in paper 2 (Strempfer *et al.*, 1996).

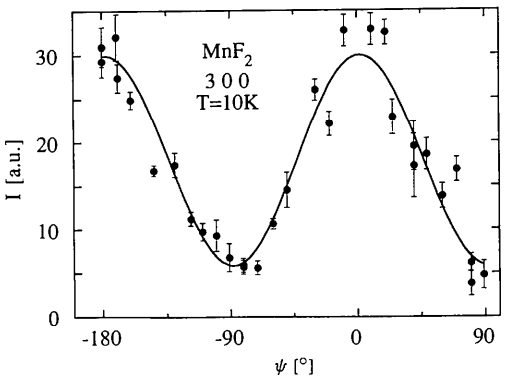

Fig. 10. Integrated intensities I of the magnetic 300 Bragg peak at $T = 10$ K and $\lambda = 1.36$ Å as a function of the angle ψ of rotation around the scattering vector. $\psi = 0$ corresponds to the spin perpendicular to the scattering plane. Measured values are given by full circles, the theoretical dependence is shown as a solid line.

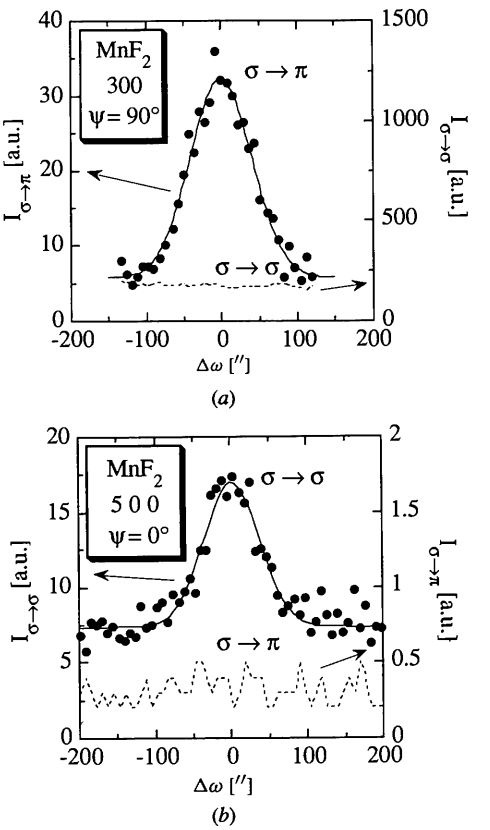

Fig. 11. (*a*) Polarization analysis of the 300 magnetic Bragg peak for $\psi = 90°$. Only $\sigma \rightarrow \pi$ scattering is observed. (*b*) Polarization analysis of the 500 magnetic Bragg peak for $\psi = 0°$. Only $\sigma \rightarrow \sigma$ scattering is observed.

If, for example, two domains with perpendicular spin direction are equally occupied, which is likely for cubic crystals or tetragonal crystals with a or b as the easy axis, the intensity variation with ψ vanishes according to (14).

8. Summary and conclusions

We have presented a new set-up for magnetic X-ray diffraction that allows a full polarization analysis of the linear polarization components. The set-up consists of a polarization monitor that measures continuously the polarization of the incident monochromatic beam and a polarization analyzer that measures the polarization after diffraction from the sample. The new design for the polarization analyzer stands out through its high versatility and efficient background suppression. The device can be employed as a conventional crystal analyzer as well as a polarization analyzer. We have shown that Si mosaic crystals can be successfully used as analyzer crystals for polarization analysis. Analyzer and monitor have been tested against each other by measuring the polarization of the incident monochromatic synchrotron beam. We showed that dynamical diffraction and thermal effects from the monochromator crystals cannot be neglected and have to be taken into account for a calculation of the degree of linear polarization. For an Si 111 double monochromator, an effective $\cos^3 2\theta$ polarization factor for the π component described our results well. For the full beam at the HASYLAB wiggler station W1, the degree of linear polarization is approximately 85%, nearly independent of photon energy. By closing vertical slits, a value of 93% can be reached. Higher values of P can be obtained by detuning the monochromator.

With the new set-up, we examined the non-resonant magnetic X-ray scattering cross section from MnF_2. An inspection of the raw data demonstrates the capabilities of the technique: count rates of up to several thousand photons s^{-1} could be obtained without the analyzer. With the analyzer, we still observed count rates of several hundred counts s^{-1}, a peak-to-background ratio of 160:1 and a Q-space resolution of 5×10^{-9} Å^{-3}. These values clearly demonstrate that, for good sample crystals (*i.e.* with narrow mosaic distribution), resonance enhancements are not necessary to obtain data that are in certain respects (namely Q-space resolution, extinction-free intensities) superior to neutron diffraction. Finally, we have examined the spin-dependent part of the non-resonant magnetic X-ray cross section: we have tested the theoretical predictions for the angular dependencies of the total intensity on the Bragg angle 2θ and the angle ψ for a rotation around the scattering vector. In a second step, we have performed a polarization analysis for two magnetic reflections 300 and 500 and two positions ψ in order to test the matrix elements of the cross section separately. Our experiments confirm the form (4) of the cross section. Finally, we point out that, for unknown spin structures, the method of measuring integrated intensities while turning the crystal around the scattering vector can be used to determine the spin direction relative to the lattice.

While today most magnetic X-ray scattering experiments deal with resonant exchange scattering, we conclude from our results that non-resonant magnetic scattering can be a quite competitive probe compared to the traditional neutron diffraction experiments for transition-metal compounds, where no significant resonance enhancement can be obtained at the K edges. For good crystals, the count rates at insertion-device beamlines are high enough to take full advantage of the high Q-space resolution and the possibility of measuring structure factors extinction free. The non-resonant magnetic X-ray scattering cross section is very rich in its angular and polarization dependencies and we have demonstrated in principle how it can be used to determine spin directions in unknown magnetic structures.

We thank W. Jauch, HMI Berlin, for providing the MnF_2 crystal and J. Ihringer, Universität Tübingen, for the closed-cycle cryostat. J. Pflüger, HASYLAB, introduced us to the use of his program *ASYSPEC* for the calculation of the wiggler spectrum. We received valuable technical help from HASYLAB engineers. We gratefully acknowledge the financial support by the Bundesministerium für Forschung und Technologie under project nos. 05-SVT1XB-0 and 03-BR4DES-2.

References

Baruchel, J., Draperi, A., El Kadiri, M., Fillion, G., Maeder, M., Molho, P. & Porteseil, J. L. (1988). *J. Phys. (Paris)*, **49**, C8, 1895–1896.

Belyakov, V. A. & Dimitrienko, V. E. (1989). *Sov. Phys. Usp.* **32**, 697–719.

Bergevin, F. de & Brunel, M. (1972). *Phys. Lett. A*, **39**, 141–142.

Bergevin, F. de & Brunel, M. (1981). *Acta Cryst.* A**37**, 314–324.

Bergevin, F. de, Stunault, A., Vettier, C., Brückel, T. & Lippert, M. (1993). HASYLAB Annual Report, pp. 623–624. HASYLAB, DESY, Hamburg, Germany.

Blume, M. (1985). *J. Appl. Phys.* **57**, 3615–3618.

Blume, M. & Gibbs, D. (1988). *Phys. Rev. B*, **37**, 1779–1789.

Bohr, J., Gibbs, D., Moncton, D. E. & D'Amico, K. L. (1986). *Physica (Utrecht)*, **140**A, 349–358.

Brückel, T., Lippert, M., Bouchard, R., Schmidt, T., Schneider, J. R. & Jauch, W. (1993). *Acta Cryst.* A**49**, 679–682.

Brückel, T., Lippert, M., Köhler, T., Schneider, J. R. & Prandl, W. (1995). *J. Magn. Magn. Mater.* **140–144**, 1743–1744.

Brunel, M. & de Bergevin, F. (1981). *Acta Cryst.* A**37**, 324–331.

Brunel, M. & de Bergevin, F. (1991). *Handbook on Synchrotron Radiation*, Vol. 3, edited by G. Brown & D. E. Moncton, pp. 536–564. Amsterdam: Elsevier.

Burkel, E. (1991). *Inelastic Scattering of X-rays with Very High Energy Resolution. Springer Tracts in Modern Physics*, No. 125. Heidelberg: Springer.

Erickson, R. A. (1953). *Phys. Rev.* **90**, 779–785.

Gibbs, D. (1992). *Synchrotron Radiat. News*, **5**, 18–23.

Gibbs, D., Blume, M., Harshman, D. R. & McWhan, D. B. (1989). *Rev. Sci. Instrum.* **60**, 1655–1660.

Gibbs, D., Harshman, D. R., Isaacs, E. D., McWhan, D. B., Mills, D. & Vettier, C. (1988). *Phys. Rev. Lett.* **61**, 1241–1244.

Gibbs, D., Moncton, D. E., D'Amico, D. L., Bohr, J. & Grier, B. H. (1985). *Phys. Rev. Lett.* **55**, 234–237.

Goldman, A. I., Mohanty, K., Shirane, G., Horn, P. M., Greene, R. L., Peters, C. J., Thurston, T. R. & Birgeneau, R. J. (1987). *Phys. Rev. B*, **36**, 5609–5612.

Grotch, H., Kazes, E., Bhatt, G. & Owen, D. A. (1983). *Phys. Rev. A*, **27**, 243–256.

Hannon, J. P., Trammell, G. T., Blume, M. & Gibbs, D. (1988). *Phys. Rev. Lett.* **61**, 1245–1248; erratum: (1989), **62**, 2644.

Hill, J. P., Feng, Q., Birgeneau, R. J. & Thurston, T. R. (1993*a*). *Phys. Rev. Lett.* **70**, 3655–3658.

Hill, J. P., Feng, Q., Birgeneau, R. J. & Thurston, T. R. (1993*b*). *Z. Phys.* B**92**, 285–305.

Hill, J. P., Thurston, T. R., Erwin, R. W., Ramstad, M. J. & Birgeneau, R. J. (1991). *Phys. Rev. Lett.* **66**, 3281–3284.

Ihringer, J. & Küster, A. (1993). *J. Appl. Cryst.* **26**, 135–137.

Isaacs, E. D., McWhan, D. B., Peters, C., Ice, G. E., Siddons, D. P., Hastings, J. B., Vettier, C. & Vogt, O. (1989). *Phys. Rev. Lett.* **62**, 1671–1674.

Jauch, W., Schneider, J. R. & Dachs, H. (1983). *Solid State Commun.* **48**, 907–909.

Jennings, L. D. (1981). *Acta Cryst.* A**37**, 584–593.

Kirfel, A., Petcov, A. & Eichhorn, K. (1991). *Acta Cryst* A**47**, 180–195.

Lippert, M., Brückel, T., Köhler, T. & Schneider, J. R. (1994). *Europhys. Lett.* **27**, 537–541.

Lovesey, S. W. (1987). *J. Phys. C*, **20**, 5625–5639.

Namikawa, K., Ando, M., Nakajima, T. & Kawata, H. (1985). *J. Phys. Soc. Jpn*, **54**, 4099–4102.

Nathans, R., Alperin, H. A., Pickart, S. & Brown, P. J. (1963). *J. Appl. Phys.* **34**, 1182–1186.

Pflüger, J. (1989). Program *ASYSPEC*. HASYLAB, DESY, Hamburg, Germany.

Platzman, P. M. & Tzoar, N. (1970). *Phys. Rev. B*, **2**, 3556–3559.

Rossad-Mignod, J. (1987). *Neutron Scattering*, Part C, edited by K. Sköld & D. L. Price, pp. 69–157. Orlando: Academic Press.

Schneider, J. R., Nagasawa, H., Berman, L. E., Hastings, J. B., Siddons, D. P. & Zulehner, W. (1989). *Nucl. Instrum. Methods*, A**276**, 636–642.

Shull, C. G., Strauser, W. A. & Wollan, E. O. (1951). *Phys. Rev.* **83**, 333–345.

Smend, F., Schaupp, D., Czerwinski, H., Millhouse, A. H. & Schenk-Strauss, H. (1985). *Nucl. Instrum. Methods,* A**241**, 290–294.

Strempfer, J., Brückel, T., Rütt, U., Schneider, J. R., Liss, K.-D. & Tschentscher, T. (1996). *Acta Cryst.* A**52**, 438–449.

Stunault, A., de Bergevin, F., Wermeille, D., Brückel, T. & Vettier, C. (1994). HASYLAB Annual Report, pp. 557–558. HASYLAB, DESY, Hamburg, Germany.

Thurston, T. R., Peters, C. J., Birgeneau, R. J. & Horn, P. M. (1988). *Phys. Rev. B*, **37** 9559–9563.